Solid State Sciences 142 (2023) 107249

Contents lists available at ScienceDirect

Solid State Sciences

journal homepage: www.elsevier.com/locate/ssscie

Synthesis and characterization of a new magnesium molybdates $Tl_{1.85}M_{0.15}Mg_2(MoO_4)_3$ (M = K, Rb) with a langbeinite type structure

Victoria G. Grossman [a,*], Maxim S. Molokeev [b,c,d], Bair G. Bazarov [a], Jibzema G. Bazarova [a]

[a] Baikal Institute of Nature Management, SB RAS, Sakhyanovoy St., 6, Ulan-Ude, 670047, Russia
[b] Kirensky Institute of Physics, Federal Research Center KSC, Siberian Branch, Academy of Sciences, 50 / 38 Akademgorodok, Krasnoyarsk, 660036, Russia
[c] Siberian Federal University, 82 Svobodniy Av., Krasnoyarsk, 660041, Russia
[d] Department of Physics, Far Eastern State Transport University, Serysheva Str. 47, Khabarovsk, 680021, Russia

ARTICLE INFO

Keywords:
Solid state method
Langbeinite
Thallium
Impedance spectroscopy

ABSTRACT

In this work we have successfully synthesized pure phases of $Tl_{1.85}M_{0.15}Mg_2(MoO_4)_3$ (M = K, Rb) langbeinite powders using the solid-state reaction method. Structural characterization was carried out via the Rietveld method on the X-ray powder diffraction data. The following unit cell parameters are calculated for $Tl_{1.85}K_{0.15}Mg_2(MoO_4)_3$: a = 10.68509(16) Å, V = 1219.93(6) Å^3, and for $Tl_{1.85}Rb_{0.15}Mg_2(MoO_4)_3$: a = 10.69463 (9) Å, V = 1223.20(3) Å^3. The electrical conductivity was studied by impedance spectroscopy in the [473–1010 K] temperature range and results show that the $Tl_{1.85}M_{0.15}Mg_2(MoO_4)_3$ (M = K, Rb) were ionic solid electrolyte conductors. Results also show that $Tl_{1.85}K_{0.15}Mg_2(MoO_4)_3$ has the highest electrical conductivity.

1. Introduction

Among the molybdates, the common structures are nasicon, and langbeinite. These structures have the same type of framework and different types of holes, cavities, tunnels for accommodation cations. So, in NASICON [1], four interstitial sites (holes in the network) are present, while langbeinite has only two. These sites are large enough to accommodate the cations that compensate the charge of the network. In the NASICON structure, the holes can be completely empty. This is not possible in the langbeinite structure. All this affects the physical and chemical properties of all these types of compounds. A characteristic feature of compounds with langbeinite structure is the presence of large one-valent cations in interstitial holes and relatively small two-valent cations in the network.

The langbeinite $K_2Mg_2(SO_4)_3$ [2,3] is the prototype of a large number of sulfates, and phosphates which have been the subject of intensive research for their potential applications in ferroelasticity, catalytic, ferroelectricity, luminescence, magnetic and optical properties [4–23].

Langbeinite-type compounds can also be used to immobilize radioactive waste [24]. Accordingly, further studies of iso- and heterovalent substitution within the cationic sites of the langbeinite structure are important.

At the present time, the molybdates with a langbeinite structure constitute a small group of compounds. Double molybdates $M_xM'_y(MoO_4)_z$ (M: univalent cations, M': uni-, di-, tri- or tetravalent cations) has been the subject of great interest because of the importance of their physical properties and potential applications, taking the example of promising laser materials [25–28], industrial catalysts [29,30] and cathodes for batteries [31–33].

The purpose of this work is to study the synthesis process, structural characteristics and ionic conductivity of compounds obtained as a result of homovalent substitution of thallium cations for rubidium and potassium in the $Tl_2Mg_2(MoO_4)_3$ compound.

2. Experimental

2.1. Synthesis

Two molybdates $Tl_{1.85}M_{0.15}Mg_2(MoO_4)_3$ (M = K, Rb) were synthesized via the ceramic route from stoichiometric amounts of preliminarily synthesized molybdates Tl_2MoO_4, $MgMoO_4$, Rb_2MoO_4 and $Hf(MoO_4)_2$ and industrial potassium molybdate (chemically pure, Red Chemist, Russia). We obtained the thallium molybdate from Tl_2CO_3 (chemically pure, Red Chemist, Russia) and MoO_3 (chemically pure, Red Chemist, Russia) at 673–823 K for 100 h. Hafnium molybdate was synthesized by reacting stoichiometric mixtures of HfO_2 (chemically pure, IGIC RAS,

* Corresponding author. Baikal Institute of Nature Management, SB RAS, Ulan-Ude 670047, Russia.
E-mail address: grossmanv@mail.ru (V.G. Grossman).

https://doi.org/10.1016/j.solidstatesciences.2023.107249
Received 20 April 2023; Received in revised form 23 June 2023; Accepted 26 June 2023
Available online 1 July 2023

Russia), and MoO_3 at 673–1023 K for 100 h. A stoichiometric mixture of $Mg(NO_3)_2 \times 6H_2O$ (chemically pure, Red Chemist, Russia) and MoO_3 was used for the synthesis of simple molybdate $MgMoO_4$ in the temperature range 673–1123 K for 100 h Rb_2MoO_4 was prepared by firing a stoichiometric mixture of Rb_2CO_3 (Lanhit, Russia) and MoO_3 (673–873 K, 80 h).

The starting reagents were well mixed and grinded in an agate mortar with a pestle and then the mixture placed in a porcelain crucible and was slowly annealed in air at 673 K for 12 h, in order to eliminate volatile compounds. Also, the choice of this starting annealing temperature was due to the fact that molybdenum oxide sublimates below the melting point.

Samples of initial molybdates for synthesis of $Tl_{1.85}M_{0.15}Mg_2(MoO_4)_3$ (M = K, Rb) in the calculated proportions were homogenized and calcined at 773, 803, and 823 K. At each stage of annealing, the samples were annealed for 48 h. After each heating stage, samples were gradually cooled to room temperature, grinded and examined by XRD method. Identical XRD results after two successive heating stages were taken as evidence that an equilibrium state had been established.

2.2. Characterization

The powder diffraction data of $Tl_{1.85}M_{0.15}Mg_2(MoO_4)_3$ (M = K, Rb) for Rietveld analysis were collected at room temperature with a Bruker D8 ADVANCE powder diffractometer (Cu-Kα radiation) and linear VANTEC detector. The step size of 2θ was 0.014°. The variable counting time (VCT) scheme was used to collect the diffraction data, the measurement time was systematically increased towards higher 2θ angles. To collect the *X*-ray data using VCT scheme, five ranges were generated on the diffraction pattern: 5°–32° (exposure per point: 1 s), 32°–59.1° (exposure per point: 2 s), 59.1°–86.1° (exposure per point: 4 s), 86.1°–113.1° (exposure per point: 8 s) and 113.1°–140.2° (exposure per point: 16 s). Total experimental time was equal to ~9 h. The esd's $\sigma(I_i)$ of all points on patterns were calculated using intensities I_i: $\sigma(I_i) = I_i^{1/2}$. The intensities and obtained esd's were further normalized, taking into account actual value of exposition time, and saved in xye-type file. So transformed powder pattern has usual view in whole 2θ range 5–140°, but all high-angle points have small esd's.

The high temperature X-ray diffraction experiments were carried out on samples using the Bruker AXS D8 Advance Diffractometer with the Anton Paar high temperature attachment HTK 16. During the experiments, the vacuum inside the chamber was better than 5 × 10-2 mbar. The step size of 2θ was 0.02°, and the counting time was 2 s per step. The experiment was carried out at temperatures of 303, 523, 573, 623, 673, 723, 773, 823 K.

The DSC/TG analysis during heating and cooling was carried out using a calorimeter NETZSCH STA 449 F1 TG/DSC/DTA (Jupiter). The sample charge was 17–18 mg, and the rate of temperature rise was 10 K/min under the Ar atmosphere. All the measurements were made in platinum crucibles. The DSC curves were calculated using a specially developed program from Netzsch.

Pellets of 10 mm of diameter and a thickness of 2 mm were prepared for conductivity measurements, by pressing fine powder at 100 bar by a PLG-12 hydraulic laboratory press at room temperature. The pellets were sintered at 773 K for 2 h in order to increase their mechanical strength. The densities of the resultant pellets were about 80–85% of theoretical ones. The disks were electroded by painting of colloid platinum on the large surfaces with subsequent annealing at 773 K for 1 h. The colloid platinum is a mixture of hexachloroplatinate (IV) ammonium $(NH_4)_2[PtCl_6]$ in toluene. Conductivity was determined by a.c. impedance measurements from 1 Hz to 1 MHz using a Z-1500J impedance analyzer at 20 K intervals on a heating and cooling cycles from 500 to 1050 K in air. Electrical conductivity σ_{total} for each temperature was calculated from:

$$\sigma_{total} = L / R_{total} \times S \quad (1)$$

where σ_{total}, L, S and R_{total} the total conductivity, the thickness of specimen, and the area of round surface and the total resistance, respectively.

3. Results and discussion

3.1. Structure refinement

Powder X-ray diffraction patterns of the molybdates $Tl_{1.85}M_{0.15}Mg_2(MoO_4)_3$ (M = K, Rb) is shown in Fig. 1. All peaks of all patterns were indexed by cubic cell ($P2_13$) with parameters close to $Tl_2Mg_2(MoO_4)_3$ [34]. Therefore, this structure was taken as starting model for Rietveld refinement which was performed using TOPAS 4.2 [34]. There are two independent Tl + sites in the structure and both of them were occupied by Tl^+/M^+ ions (M = K, Rb) (Fig. 2). The Tl^+:M^+ ratio was refined in both sites independently. Refinements were stable and gave low *R*-factors (Table 1, Fig. 2). Coordinates of atoms and main bond lengths are in Table 2 and Table 3 respectively.

The base of the crystal structure of the molybdate is a loose three-dimensional mixed framework built of alternating and corner-sharing MoO_4 tetrahedra and MgO_6 octahedra. As a result of this corner sharing, large ellipsoidal interstices are formed in the framework, each interstice accommodating two thallium atoms. The projection of the structure along axis *c* is shown in the figure.

The crystallographic data are deposited in Cambridge Crystallographic Data Centre (CCDC # 2256033–2256034). The data can be downloaded from the site (www.ccdc.cam.ac.uk/data_request/cif).

3.2. HT XRPD

All peaks were indexed by cubic cell ($P2_13$) with parameters close to the phase under consideration. Le Bail profile fitting was performed using TOPAS 4.2 [35]. Refinements were stable and gave low *R*-factors (Table 4, Fig. 1S). Heating produces only slight changes in the XRD patterns of the samples. Reflections from $Tl_{1.85}Rb_{0.15}Mg_2(MoO_4)_3$ shift only gradually to smaller angles (Fig. 1S). The evolution of the volume and unit cell parameters of $Tl_{1.85}Rb_{0.15}Mg_2(MoO_4)_3$ as a function of temperature is plotted in Fig. 3.

Below 823 K temperature, the compound undergoes no phase transitions. The cell parameter *a* and volume increase from 10.6844(3) to 10.80180(19) Å and 1219.69(9) to 1260.34(7), respectively.

3.3. Thermal analysis

In order to study the thermal behavior of the $Tl_{1.85}M_{0.15}Mg_2(MoO_4)_3$ (M = K, Rb) samples, DSC analyses were undertaken in the temperature range of 298–1180 K under argon atmosphere at 10 K/min (Figs. 4 and 5). In the temperature interval no mass loss occurred while heating of molybdates. In the DSC heating curves of powders, one endothermal effect at the ones temperature ~ 1139 K for $Tl_{1.85}K_{0.15}Mg_2(MoO_4)_3$ and ~ 1152 K for $Tl_{1.85}Rb_{0.15}Mg_2(MoO_4)_3$ were registered, corresponding of melting temperature. Under cooling conditions, several thermal effects were observed (Figs. 4 and 5).

3.4. Electrical properties

The Nyquist plots use for absolute estimate the electrical nature of the compounds like impedance of grain, grain boundaries and electrodes. The complex impedance properties of the sample are characterized by the generation of semicircular arcs whose pattern of progression varies in respect of temperature. High frequency and low frequency semicircles represent grain and electrode contribution respectively, while intermediate frequency semi-circle represents the

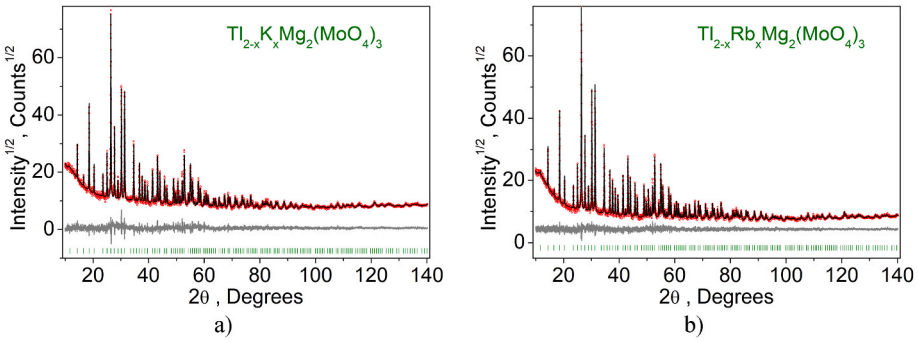

Fig. 1. Difference Rietveld plot of $Tl_{2-x}M_xMg_2(MoO_4)_3$: M = K (a); M = Rb (b).

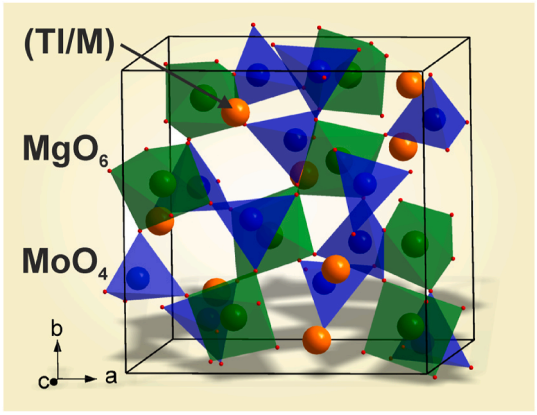

Fig. 2. Crystal structure of Tl2-*x*M*x*Mg2(MoO4)3.

Table 1
Main parameters of processing and refinement of the $Tl_{1.85}M_{0.15}Mg_2(MoO_4)_3$ (M = K, Rb) samples.

M	Space Group	Cell parameters (Å), Cell Volume (Å3)	*Rwp*, *Rp*, R_B, $\chi 2$
K	$P2_13$	a = 10.68509(16), V = 1219.93(6)	6.82, 6.81, 2.97, 1.56
Rb	$P2_13$	a = 10.69463(9), V = 1223.20(3)	5.53, 5.3, 1.91, 1.24

grain boundary contribution [35].

Figs. 5 and 6 show the Nyquist diagrams (-Z'' (Ω) vs (Z' (Ω)) for the two synthesized samples registered in the [473–1010 K] range. The capacitance values can be obtained using the relation, $\omega RC = 1$, where, $\omega = 2f$, f is the frequency in Hz at maxima) is the angular frequency, R is the arc magnitude. Grains and grain boundaries have a capacitance of pF and nF order respectively, while electrode-sample interface has a capacitance of μF order [36]. The presence of semicircular arcs above 690 K temperature represents the electrical processes in the material, which may occur because of the contributions from grains and grain boundaries in the bulk material. Capacitance values for this high frequency semicircle were in the range 10^{-11}–10^{-10} F, typical for grain boundary resistances in oxide systems [37]. The separation of total resistance into bulk and grain boundary components was not possible. As temperature increases, the radius of the semicircle decreases in all composites in the frequency region 100 Hz−100 kHz. This indicates temperature dependent on relaxation process. A typical impedance spectrum (Figs. 6 and 7) consists of a low frequency tail indicating that the conductivity is mainly ionic.

The temperature dependence of the electrical conductivity of $Tl_{1.85}K_{0.15}Mg_2(MoO_4)_3$ and $Tl_{1.85}Rb_{0.15}Mg_2(MoO_4)_3$ is shown in Fig. 8 in

Table 2
Fractional atomic coordinates and isotropic displacement parameters (Å2) of $Tl_{1.85}M_{0.15}Mg_2(MoO_4)_3$ (M = K, Rb).

Atom	*x*	*Y*	*z*	*Biso*	*Occ.*
M = K					
Tl1	0.1743(2)	0.1743(2)	0.1743(2)	2.43(12)	0.800(14)
K1	0.1743(2)	0.1743(2)	0.1743(2)	2.43(12)	0.200(14)
Tl2	0.9501(2)	0.9501(2)	0.9501(2)	5.68(19)	0.997(15)
K2	0.9501(2)	0.9501(2)	0.9501(2)	5.68(19)	0.003(15)
Mg1	0.3881(10)	0.3881(10)	0.3881(10)	0.8(3)	1
Mg2	0.6617(10)	0.6617(10)	0.6617(10)	0.8(3)	1
Mo	0.4748(3)	0.6991(3)	0.3755(3)	1.12(11)	1
O1	0.473(3)	0.567(3)	0.312(3)	4.7(8)	1
O2	0.533(3)	0.803(3)	0.253(3)	4.8(7)	1
O3	0.310(2)	0.769(2)	0.369(2)	3.5(8)	1
O4	0.550(2)	0.718(2)	0.535(3)	3.3(7)	1
x = Rb					
Tl1	0.17464(15)	0.17464(15)	0.17464(15)	2.63(9)	0.836(17)
Rb1	0.17464(15)	0.17464(15)	0.17464(15)	2.63(9)	0.164(17)
Tl2	0.95136(19)	0.95136(19)	0.95136(19)	4.93(14)	0.859(17)
Rb2	0.95136(19)	0.95136(19)	0.95136(19)	4.93(14)	0.141(17)
Mg1	0.3867(8)	0.3867(8)	0.3867(8)	0.9(2)	1
Mg2	0.6658(9)	0.6658(9)	0.6658(9)	1.8(2)	1
Mo	0.4756(2)	0.7012(2)	0.3760(2)	1.03(8)	1
O1	0.473(3)	0.549(3)	0.335(3)	7.3(8)	1
O2	0.538(2)	0.789(2)	0.256(2)	3.8(5)	1
O3	0.311(3)	0.755(2)	0.397(2)	5.8(7)	1
O4	0.561(3)	0.728(2)	0.532(3)	6.8(9)	1

Table 3
Main bond lengths (Å) of $Tl_{1.85}M_{0.15}Mg_2(MoO_4)_3$ (M = K, Rb).

x = K			
Tl1–O3^{i}	3.322(21)	Tl1–O4^{i}	3.046(24)
K1–O3^{i}	3.322(21)	K1–O4^{i}	3.046(24)
Tl2–O1^{ii}	2.817(32)	Tl2–O2^{iii}	3.380(32)
K2–O1^{ii}	2.817(32)	K2–O2^{iii}	3.380(32)
Mg1–O1	2.266(33)	Mg1–O2^{iv}	1.952(33)
Mg2–O3^{ii}	1.779(23)	Mg2–O4	1.902(29)
Mo–O1	1.566(32)	Mo–O3	1.914(21)
Mo–O2	1.825(32)	Mo–O4	1.894(30)
x = Rb			
Tl1–O2^{iv}	3.389(21)	Tl1–O3^{i}	3.066(21)
Tl1–O4^{i}	3.124(31)	Rb1–O2^{iv}	3.389(21)
Rb1–O3^{i}	3.066(21)	Rb1–O4^{i}	3.124(31)
Tl2–O1^{ii}	3.071(32)	Tl2–O2^{iii}	3.476(21)
Rb2–O1^{ii}	3.071(32)	Rb2–O2iii	3.476(21)
Mg1–O1	2.042(33)	Mg1–O2^{iv}	2.017(23)
Mg2–O3^{ii}	1.892(25)	Mg2–O4	1.935(32)
Mo–O1	1.685(32)	Mo–O4	1.923(31)
Mo–O2	1.724(21)	Mo–O3	1.865(31)

Symmetry codes: (i) -*x*+1/2, -*y*+1, *z*+1/2; (ii) -*y*+3/2, -*z*+1, *x*+1/2; (iii) -*x*+3/2, -*y*+2, *z*+1/2; (iv) -*z*+1/2, -*x*+1, *y*+1/2.

Table 4
Main parameters of processing and refinement of the samples.

T, K	Space Group	Cell parameters (Å), Cell Volume (Å3)	Rwp, Rp, χ2
303	$P2_13$	$a = 10.6844(3)$, $V = 1219.69(9)$	7.48, 5.78, 1.83
523	$P2_13$	$a = 10.7372(3)$, $V = 1237.86(9)$	7.71, 5.96, 1.91
573	$P2_13$	$a = 10.7441(3)$, $V = 1240.26(10)$	7.62, 5.91, 1.88
623	$P2_13$	$a = 10.7521(3)$, $V = 1243.02(12)$	8.05, 6.25, 2.00
673	$P2_13$	$a = 10.7706(5)$, $V = 1249.46(16)$	9.08, 7.14, 2.23
723	$P2_13$	$a = 10.7860(2)$, $V = 1254.82(9)$	7.33, 5.65, 1.82
773	$P2_13$	$a = 10.7918(2)$, $V = 1256.85(7)$	7.51, 5.79, 1.86
823	$P2_13$	$a = 10.80180(19)$, $V = 1260.34(7)$	6.96, 5.40, 1.71

an Arrhenius plot. A high conductivity jump of about three orders of magnitude in the Arrhenius plot is observed above 700 K for $Tl_{1.85}K_{0.15}Mg_2(MoO_4)_3$ and about four orders for $Tl_{1.85}Rb_{0.15}Mg_2(MoO_4)_3$. Such a jump of conductivity is due not only to a gradual increase in temperature, but also to an increase in the parameters and volume of the unit cell (Table 4). Table 4 shows that with an increase in temperature from 303 to 823 K, the parameter a increases by 0.1174 Å, and the unit cell volume increases by 40.65 Å3. The dependencies have two linear parts with different slopes. A change in the slope is observed near the temperature of transition. Both below and above the phase transition, the dependences are adequately described by the Arrhenius–Frenkel law. The observed processes are thermally activated. The activation energies of conductivity for $Tl_{1.85}K_{0.15}Mg_2(MoO_4)_3$ in the temperature region above the phase transition point (730–1000 K, cooling mode for pellet) is estimated to be $E_a = 1.55$ eV. The activation energy of conductivity for a tablet $Tl_{1.85}Rb_{0.15}Mg_2(MoO_4)_3$ (cooling mode at 830–1000 K) is estimated to be $E_a = 0.74$ eV. Molybdates $Tl_{1.85}K_{0.15}Mg_2(MoO_4)_3$ and $Tl_{1.85}Rb_{0.15}Mg_2(MoO_4)_3$ have a low conductivity ($\sim 10^{-8}$ S/cm at 500 K), as a result of a phase transition it passes into the superionic state ($\sim 10^{-3}$ S/cm at 900 K). Based on the structure analysis provided in this paper the ionic conductivity observed in $Tl_{1.85}K_{0.15}Mg_2(MoO_4)_3$ and $Tl_{1.85}Rb_{0.15}Mg_2(MoO_4)_3$ is most probably due to monovalent thallium, potassium and rubidium cations mobility. The multiply charged Mg^{2+}, Mo^{6+} cations, which are part of the crystal framework, form stronger chemical bonds with oxygen than singly charged. Tl^+, K^+/Rb^+ cations located in ellipsoidal interstices. This indicates higher mobility of Tl^+ cations in comparison with the cations Mg^{2+}, Mo^{6+}. Tl^+, K^+/Rb^+ cations have an anomalously large vibration amplitude (Table 2) and interact electrostatically with the negatively charged framework, which indicates their high mobility.

In the work [38], the conductivity of $Tl_2Mg_2(MoO_4)_3$ was not determined, so we studied its in order to compare it with the conductivity of the compounds we obtained. Fig. 9 shows the variation of logσ versus 1000/T for $Tl_2Mg_2(MoO_4)_3$. Conductivity at 773 K for $Tl_{1.85}K_{0.15}Mg_2(MoO_4)_3$ is 5.7×10^{-4} S/cm, $Tl_{1.85}Rb_{0.15}Mg_2(MoO_4)_3$ – 2.7×10^{-4} S/cm and for $Tl_2Mg_2(MoO_4)_3$ – 3.9×10^{-4} S/cm. On the one side, doping $Tl_2Mg_2(MoO_4)_3$ with rubidium led to some decrease in conductivity over the entire temperature range. On the other hand, the conductivity of the sample $Tl_2Mg_2(MoO_4)_3$ doped with potassium increased, but only slightly. The obtained ionic conductivity of $Tl_{1.85}M_{0.15}Mg_2(MoO_4)_3$ (M = K, Rb) at 773 K in this study is higher for one orders than $K_2Mg_2(SO_4)_3$:xGd (x = 0.5 mol %), which also has a langbeinite structure, 4.14×10^{-5} S/cm at 733 K [39].

4. Conclusion

In the present study, $Tl_{1.85}M_{0.15}Mg_2(MoO_4)_3$ (M = K, Rb) and $Tl_2Mg_2(MoO_4)_3$ were synthesized by standard solid state reaction at 823 K. X-ray powder diffraction studies show that this compounds crystallizes in the cubic symmetry with the $P2_13$ space group and the unit cell parameters are: a = 10.68509(16) Å, V = 1219.93(6) Å^3 for $Tl_{1.85}K_{0.15}Mg_2(MoO_4)_3$, and for $Tl_{1.85}Rb_{0.15}Mg_2(MoO_4)_3$: a = 10.69463 (9) Å, V = 1223.20(3) Å^3. The complex impedance plots were obtained using Z-1500J impedance analyzer in frequency range from 1 Hz to 1 MHz between 473 K and 1010 K. The Arrhenius plots of

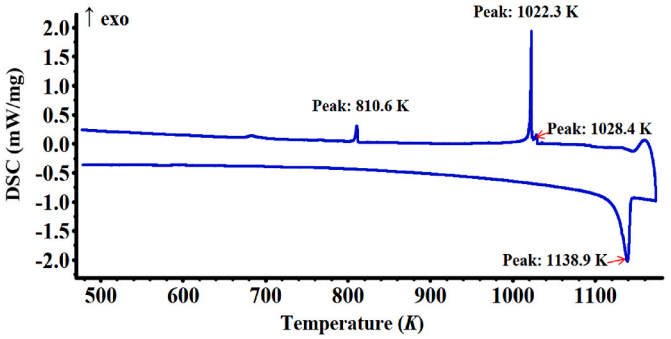

Fig. 4. The DSC heating and cooling curves of sample of $Tl_{1.85}K_{0.15}Mg_2(MoO_4)_3$.

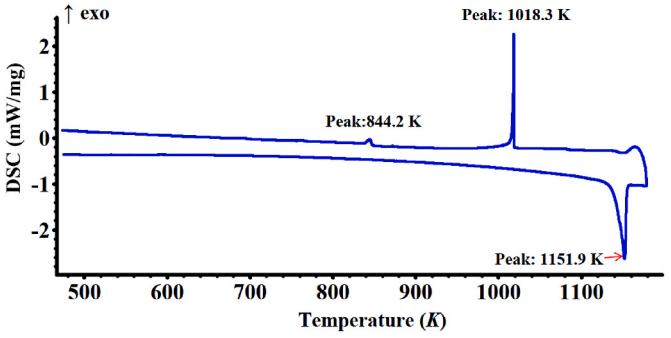

Fig. 5. The DSC heating and cooling curves of sample of $Tl_{1.85}Rb_{0.15}Mg_2(MoO_4)_3$.

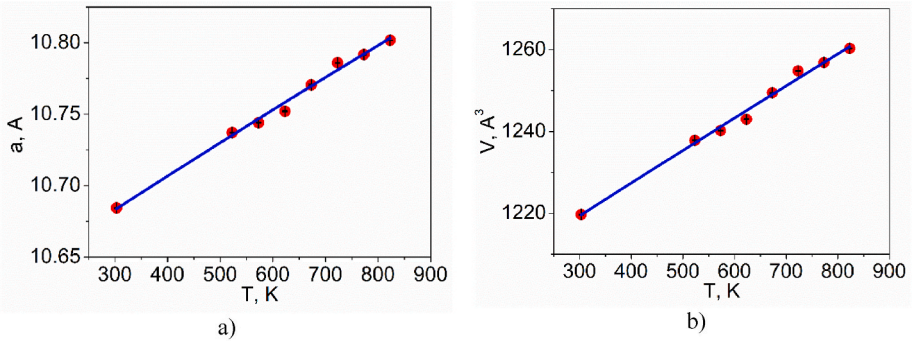

Fig. 3. a) Linear cell volume dependence V(T); b) Linear cell parameter dependence a(T).

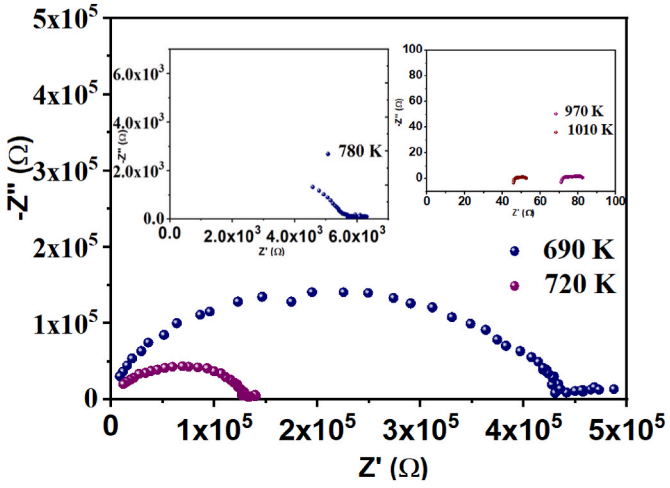

Fig. 6. Impedance hodographs for $Tl_{1.85}K_{0.15}Mg_2(MoO_4)_3$.

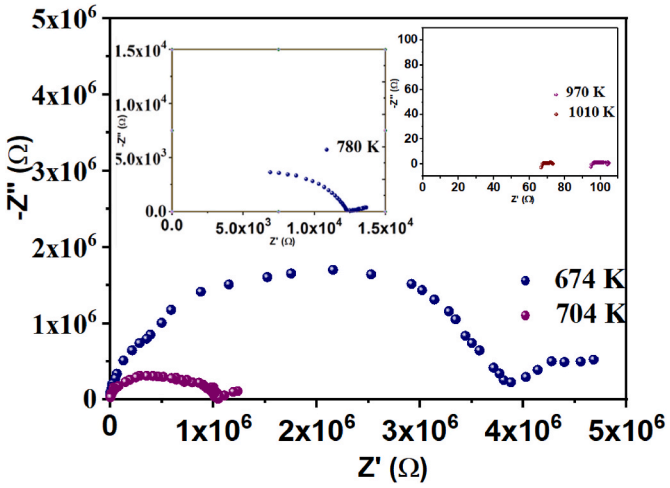

Fig. 7. Impedance hodographs for $Tl_{1.85}Rb_{0.15}Mg_2(MoO_4)_3$.

$Tl_{1.85}M_{0.15}Mg_2(MoO_4)_3$ (M = K, Rb) and $Tl_2Mg_2(MoO_4)_3$ show a jump in conductivity. $Tl_{1.85}K_{0.15}Mg_2(MoO_4)_3$ presents a conductivity value equal to 5.7 × 10^{-4} S/cm at 773 K, with E_a equal to 1.55 eV. For $Tl_{1.85}Rb_{0.15}Mg_2(MoO_4)_3$, ionic conductivity of 2.7 × 10^{-4} is observed at the same temperature with E_a equal to 0.74 eV.

Funding

This work was supported by the state order of BINM SB RAS (0273-2021-0008). Research was conducted using equipment of the CCU BINM SB RAS. Some experiments were obtained with use the analytical equipment of analytical equipment of Krasnoyarsk Regional Center of Research Equipment of Federal Research Center "Krasnoyarsk Science Center SB RAS". M.S. Molokeev's work was carried out within the framework of the Strategic Academic Leadership Program "Priority-2030″ for the Siberian Federal University.

CRediT authorship contribution statement

Victoria G. Grossman: Investigation, Writing – original draft, preparation, Writing – review & editing. **Maxim S. Molokeev:** Refinement of the structure by the Rietveld method and co-wrote the paper. **Bair G. Bazarov:** Resources. **Jibzema G. Bazarova:** Resources.

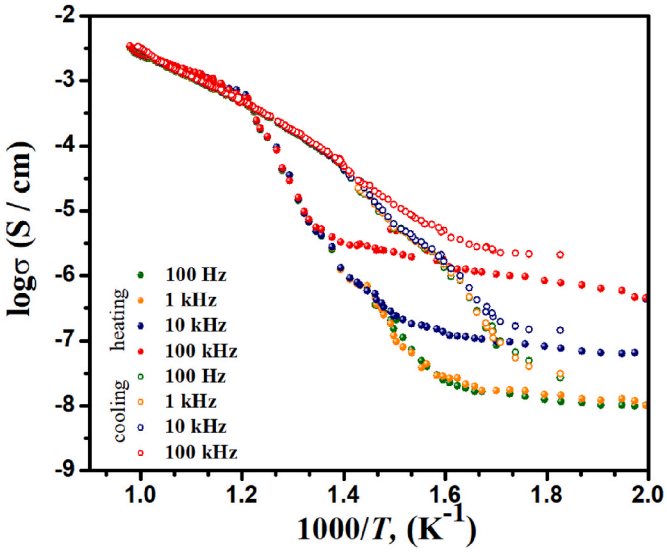

Fig. 9. Arrhenius plots for total electrical conductivity of $Tl_2Mg_2(MoO_4)_3$.

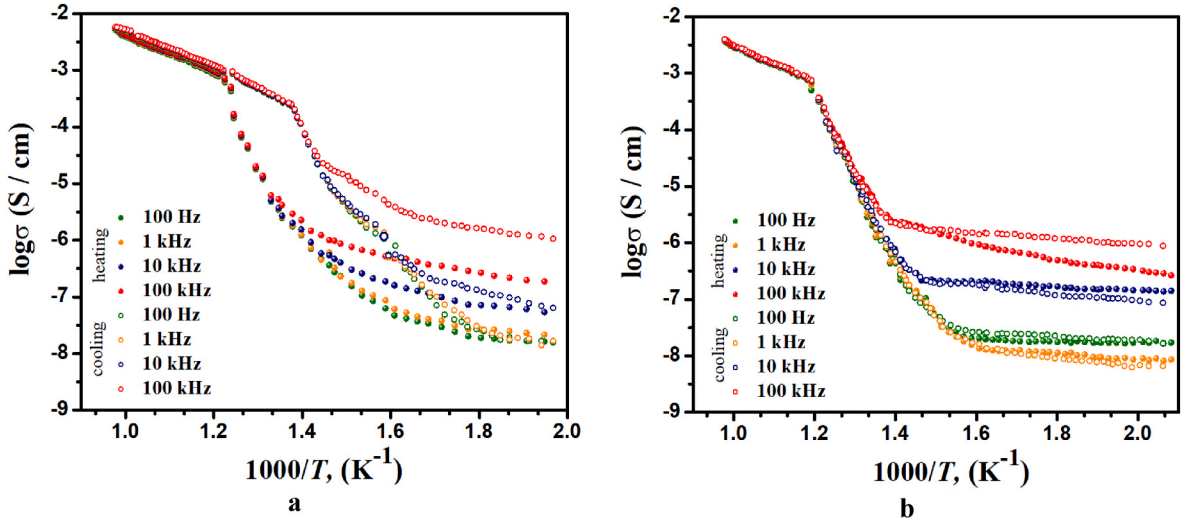

Fig. 8. Arrhenius plots for total electrical conductivity of $Tl_{1.85}K_{0.15}Mg_2(MoO_4)_3$ (a) and $Tl_{1.85}Rb_{0.15}Mg_2(MoO_4)_3$ (b).

Declaration of competing interest

The authors declare that they have no known competing financial interests or personal relationships that could have appeared to influence the work reported in this paper.

Data availability

Data will be made available on request.

References

[1] K.K. Rangan, J. Gopalakrishnan, New titanium-vanadium phosphates of nasicon and langbeinite structures, and differences between the two structures toward deintercalation of alkali metal, J. Solid State Chem. 109 (1) (1994) 116–121, https://doi.org/10.1006/jssc.1994.1080.

[2] Refinement of the crystal structure of langbeinite, $K_2Mg_2(SO_4)_3$, Neues Jahrb. Mineral. Monatsh. (1979) 182–188.

[3] A. Zemann, J. Zemann, Die kristallstructure von Langbeinit, $K_2Mg_2(SO_4)_3$, Acta Crystallogr. 10 (6) (1957) 409–413.

[4] T. Hikita, S. Sato, H. Sekiguchi, T. Ikeda, Heat capacity studies of phase transitions in langbeinites II. $K_2Mg_2(SO_4)_3$, J. Phys. Soc. Jpn. 42 (1977) 1656–1659.

[5] D. Speer, E. Salje, Phase transitions in langbeinites I: crystal chemistry and structures of K-double sulfates of the langbeinite type $M_2^{2+}K_2(SO_4)_3$, M^{2+} = Mg, Ni, Co, Zn, Ca, Phys. Chem. Miner. 13 (1986) 17–24.

[6] Z.J. Zhang, J.L. Yuan, H.H. Chen, Xin-Xin Yang, Jingtai Zhao, Guo-Bin Zhang, C. S. Shi, Vacuum ultraviolet spectroscopic properties of rare earth (*Re*) (*Re* = Eu, Tb, Dy, Sm, Tm)-Doped $K_2GdZr(PO_4)_3$ phosphate, Solid State Sci. 11 (2) (2009) 549–555, https://doi.org/10.1016/j.solidstatesciences.2008.07.008.

[7] Y. Shen, Y.i. Yang, S. Zhao, X. Li, Q. Ding, Y. Li, S. Liu, Z. Lin, J. Luo, A Langbeinite type yttrium phosphate $LiCs_2Y_2(PO_4)_3$, Inorg. Chem. 57 (21) (2018) 13087–13091, https://doi.org/10.1021/acs.inorgchem.8b02491.

[8] B. Lajmi, M. Hidouri, A. Wattiaux, L. Fournés, J. Darriet, M. Ben Amara, Crystal structure, Mössbauer spectroscopy, and magnetic properties of a new potassium iron oxyphosphate $K_{11}Fe_{15}(PO_4)_{18}O$ related to the Langbeinite-like compounds, J. Alloys Compd. 361 (1–2) (2003) 77–83, https://doi.org/10.1016/S0925-8388(03)00412-2.

[9] S.-R. Zhang, D. Zhao, Y.-C. Fan, Z. Ma, Y.-L. Xue, Y.-N. Li, Color tunability and energy transfer studies of a new Eu^{3+} doped langbeinite-type phosphate phosphor for lighting applications, J. Solid State Chem. 279 (2019), 120965, https://doi.org/10.1016/j.jssc.2019.120965.

[10] R. Kumar, R. Shanker, R.K. Kotnala, S. Chawla, Luminomagnetic $K_2Gd_{1-x}Zr(PO_4)_3$:Tbx^{3+} phosphor with intense green fluorescence and paramagnetism, Phys. Status Solidi Appl. Mater. Sci. 210 (9) (2013) 1933–1937, https://doi.org/10.1002/pssa.201329087.

[11] M. Kahrizi, M.O. Steinitz, Phase transitions and thermal expansion in langbeinite type compounds, Solid State Commun. 66 (4) (1988) 375–378, https://doi.org/10.1016/0038-1098(88)90860-5.

[12] J. Isasi, A. Daidouh, Synthesis, structure and conductivity study of new monovalent phosphates with the langbeinite structure, Solid State Ionics 133 (2000) 303–313, https://doi.org/10.1016/S0167-2738(00)00677-9.

[13] A.I. Orlova, I.G. Trubach, V.S. Kurazhkovskaya, P. Pertierra, M.A. Salvadó, S. García-Granda, S.A. Khainakov, J.R. García, Synthesis, characterization, and structural study of $K_2FeZrP_3O_{12}$ with the langbeinite structure, J. Solid State Chem. 173 (2003) 314–318, https://doi.org/10.1016/S0022-4596(03)00101-4.

[14] J.J. Carvajal, A. Aznar, R. Solé, J. Gavaldà, J. Massons, X. Solans, M. Aguiló, F. Díaz, Growth and structural characterization of $Rb_2Ti_{1.01}Er_{0.99}(PO_4)_3$, Chem. Mater. 15 (1) (2003) 204–211.

[15] S. Chen, S. Hoffmann, K. Weichert, J. Maier, Y. Prots, J.-T. Zhao, R. Kniep, Li $(H2O)_{2-x}[Zr_2(PO_4)_3]$: a Li-filled langbeinite variant (x=0) as a precursor for a metastable dehydrated phase (x=2), Chem. Mater. 23 (6) (2011) 1601–1606, https://doi.org/10.1021/cm103487w.

[16] Y. Shen, Y.I. Yang, S. Zhao, X. Li, Q. Ding, Y. Li, S. Liu, Z. Lin, J. Luo, A Langbeinite-type yttrium phosphate $LiCs_2Y_2(PO_4)_3$, Inorg. Chem. 57 (21) (2018) 13087–13091, https://doi.org/10.1021/acs.inorgchem.8b02491.

[17] T. Hikita, Y. Chubachi, T. Ikeda, X-ray study of the phase transition in $K_2Mn_2(SO_4)_3$, J. Phys. Soc. Jpn. 44 (2) (1978) 525–528, https://doi.org/10.1143/JPSJ.44.525.

[18] M. Hidouri, M.L. López, C. Pico, A. Wattiaux, M.B. Amara, Synthesis and characterization of a new iron phosphate $KSrFe_2(PO_4)_3$ with a langbeinite type structure, J. Mol. Struct. 1030 (2012) 145–148, https://doi.org/10.1016/j.molstruc.2012.04.002.

[19] B. Lajmi, M. Hidouri, A. Wattiaux, L. Fournés, J. Darriet, M. Ben Amara, Crystal structure, Mössbauer spectroscopy, and magnetic properties of a new potassium iron oxyphosphate $K_{11}Fe_{15}(PO_4)_{18}O$ related to the Langbeinite-like compounds, J. Alloys Compd. 361 (1–2) (2003) 77–83, https://doi.org/10.1016/S0925-8388(03)00412-2.

[20] S.-R. Zhang, D. Zhao, Y.-C. Fan, Z. Ma, Y.-L. Xue, Y.-N. Li, Color tunability and energy transfer studies of a new Eu^{3+} doped langbeinite-type phosphate phosphor for lighting applications, J. Solid State Chem. 279 (2019), 120965, https://doi.org/10.1016/j.jssc.2019.120965.

[21] R. Kumar, R. Shanker, R.K. Kotnala, S. Chawla, Luminomagnetic $K_2Gd_{1-x}Zr(PO_4)_3$:Tb_x^{3+} phosphor with intense green fluorescence and paramagnetism, Phys. Status Solidi Appl. Mater. Sci. 210 (9) (2013) 1933–1937.

[22] M. Kahrizi, M.O. Steinitz, Phase transitions and thermal expansion in langbeinite type compounds, Solid State Commun. 66 (4) (1988) 375–378, https://doi.org/10.1016/0038-1098(88)90860-5.

[23] H. Bellefqih Aatiq, A. Marchoud, R. Fakhreddine, N. Boudar, R. Tigha, Structure of two new $K_2SnX(PO_4)_3$ (*X* = Cr, In) langbeinite-type phases, J. Mater. Environ. Sci. 8 (2017) 2940–2945.

[24] A.I. Orlova, A.K. Koryttseva, E.E. Loginova, A family of phosphates of langbeinite structure. Crystal-chemical aspect of radioactive waste immobilization, Radiochemistry 53 (2011) 51–62, https://doi.org/10.1134/S1066362211010073.

[25] L. Li, Y. Yu, G. Wang, L. Zhang, Crystal growth, spectroscopic properties and energy levels of Cr^{3+}:$Li_2Mg_2(WO_4)_3$: a candidate for broadband laser application, RSC Adv. 4 (2014), 37041.

[26] H. Ren, H. Li, Y. Zou, H. Deng, Z. Peng, T. Ma, Sh Ding, Growth and properties of Pr^{3+}-doped $NaGd(MoO_4)_2$ single crystal: a promising InGaN laser-diode pumped orange-red laser crystal, J. Lumin. 249 (2022), 119034, https://doi.org/10.1016/j.jlumin.2022.119034.

[27] P. Loiko, A. Pavlyuk, S. Slimi, R.M. Solé, E.B. Salem, E. Dunina, A. Kornienko, P. Camy, U. Griebner, V. Petrov, F. Díaz, M. Aguiló, X. Mateos, Growth, spectroscopy and laser operation of monoclinic Nd:$CsGd(MoO_4)_2$ crystal with a layered structure, J. Lumin. 231 (2021), 117793, https://doi.org/10.1016/j.jlumin.2020.117793.

[28] Y. Zhang, H. Cong, H. Jiang, J. Li, J. Wang, Flux growth, structure, and physical characterization of new disordered laser crystal $LiNd(MoO_4)_2$, J. Cryst. Growth 423 (2015) 1–8, https://doi.org/10.1016/j.jcrysgro.2015.04.015.

[29] R. Nasri, T. Larbi, H. Khemir, M. Amlouk, M.F. Zid, Photocatalytic efficiency of $Na_4Co(MoO_4)_3$ for the degradation of industrial azo dye under solar irradiation, Inorg. Chem. Commun. 119 (2020), 108113, https://doi.org/10.1016/j.inoche.2020.108113.

[30] R. Nasri, T. Larbi, H. Khemir, M. Amlouk, M.F. Zid, Synthesis, crystal structure and photocatalytic activity of a new $NaLi_{1.07}Co_{2.94}(MoO_4)_5$ nanoparticles for real tannery wastewater treatment, J. Solid State Chem. 307 (2022), 122838, https://doi.org/10.1016/j.jssc.2021.122838.

[31] S.R.S. Prabaharan, M.S. Michael, S. Ramesh, K.M. Begam, Synthesis and redox properties of $Li_xNi_2(MoO_4)_3$: a new 3-V class positive electrode material for rechargeable lithium batteries, J. Electroanal. Chem. 570 (2004) 107, https://doi.org/10.1016/j.jelechem.2004.03.022.

[32] S.R.S. Prabaharan, S. Ramesh, M.S. Michael, K.M. Begam, Characterization of soft-combustion-derived NASICON-type $Li_2Co_2(MoO_4)_3$ for lithium batteries, Mater. Chem. Phys. 87 (2004) 318–326, https://doi.org/10.1016/j.matchemphys.2004.05.041.

[33] S.R.S. Prabaharana, A. Fauzi, M.S. Michael, K.M. Begam, New NASICON-type $Li_2Ni_2(MoO_4)_3$ as a positive electrode material for rechargeable lithium batteries, Solid State Ionics 171 (2004) 157–165, https://doi.org/10.1016/j.ssi.2004.05.001.

[34] Bruker AXS TOPAS V4: General Profile and Structure Analysis Software for Powder Diffraction Data. – User's Manual, Bruker AXS, Karlsruhe, Germany, 2008.

[35] G.B. Balazs, R.S. Glass, Ac impedance studies of rare earth oxide doped ceria, Solid State Ionics 76 (1995) 155–162.

[36] K.C. Anjaneya, G.P. Nayaka, J. Manjanna, G. Govindaraj, K.N. Ganesha, Studies on structural, morphological and electrical properties of $Ce_{0.8}Ln_{0.2}O_{2-\delta}$ (Ln = Y^{3+}, Gd^{3+}, Sm^{3+}, Nd^{3+} and La^{3+}) solid solutions prepared by citrate complexation method, J. Alloys Compd. 585 (5) (2014) 594–601, https://doi.org/10.1016/j.jallcom.2013.09.101.

[37] J.T.S. Irvine, D.C. Sinclair, A.R. West, Electroceramics: characterization by impedance spectroscopy, Adv. Mater. 2 (1990) 132–138, https://doi.org/10.1002/adma.19900020304.

[38] B.G. Bazarov, T.T. Bazarova, S.I. Arkhincheeva, K.N. Fedorov, Z.G. Bazarova, R. F. Klevtsova, L.A. Glinskaya, Double molybdate $Tl_2Mg_2(MoO_4)_3$: synthesis, structure, and properties, J. Neorg. Chem. 51 (10) (2006) 1677–1680.

[39] A. Souamti, D.B.H. Chehimi, Effects of Gd_2O_3 doping on the structure and the conduction mechanism of $K_2Mg_2(SO_4)_3$ langbeinite ceramics: a comparative study, Mater. Sci. Eng., B 265 (2021), 115040, https://doi.org/10.1016/j.mseb.2020.115040.